Engineering Analysis with Boundary Elements 33 (2009) 1246–1257

Contents lists available at ScienceDirect

Engineering Analysis with Boundary Elements

journal homepage: www.elsevier.com/locate/enganabound

Solution for wave propagation through a circular cylinder mounted on different topography ripple-bed profile shoals using DRBEM

Sung-Shan Hsiao [a], Chun-Ming Chang [a], Chih-Chung Wen [b,*]

[a] Department of Harbor and River Engineering, National Taiwan Ocean University, No. 2, Pei-Ning Road, Keelung 20224, Taiwan
[b] Department of Safety, Health and Environmental Engineering, Hungkuang University, No. 34, Chung-Chie Road, Shalu, Taichung 43302, Taiwan

ARTICLE INFO

Article history:
Received 26 February 2009
Accepted 4 June 2009
Available online 15 July 2009

Keywords:
Modified mild-slope equation
Dual reciprocity boundary element method
Homma's island
Conical island
Wave model
Ripple-beds

ABSTRACT

In this paper, the dual reciprocity boundary element method wave model that is governed by a modified mild-slope equation is developed. Instead of addressing the infinite boundary condition, the model automatically satisfies the Sommerfeld radiation condition. This work examines the effects of both the bottom curvature and the slope-squared terms. The conducted numerical experiments have a topography that is composed of a cylinder mounted on two kinds of basic shoal: types 1 and 2 cubic. In addition, numerical experiments that combine two cubic type islands with ripple-beds are performed.

The results show that the curvature term dominates the calculation of the sinusoidal-varying topography; even a disturbance in the topography is insignificant. In contrast to smooth topographies, the bottom curvature and the slope-squared terms are not dominant. Thus, the extended terms can be neglected if the seabed is smooth and gentle. When the topographies are combined with ripple-beds, the difference in the dimensionless wave amplitudes along the sidewall of the types 1 and 2 cubic islands is found to be 2.9 and 3.02, respectively. According to our study of cubic islands that are combined with ripple-beds, we can conclude with certainty that even though the variation of the seabed is very slight, the curvature and the slope-squared terms cannot be neglected for an uneven bottom.

Crown Copyright © 2009 Published by Elsevier Ltd. All rights reserved.

1. Introduction

The mild-slope equation that has been derived by Berkhoff [1] is a valid method to simulate the linear wave propagation from deep to shallow water. The assumption of $|\nabla h|kh \ll 1$ in the mild-slope equation means that the higher-order bottom-effect terms are neglected in the original derivation of Berkhoff's procedure. Motivated in part by significant engineering applications, much of the relevant existing literature has concentrated on rapidly varying or steep topography.

In terms of the reflection coefficients, Booij [2] has compared the numerical results of the mild-slope equation with the finite element model results for the case of a monochromatic wave propagating over a plane slope and has concluded that the mild-slope equation is sufficiently accurate up to a bottom slope of 1:3. However, it has been pointed out in several investigations that the classic mild-slope equation fails to produce adequate approximations for certain types of bathymetry, such as offshore reefs or bars. Numerous studies have been conducted to improve the applicability of the mild-slope equation for rapidly and relatively steep bathymetry. Using Green's identity, Kirby [3] has developed a time-dependent extension of Berkhoff's mild-slope equation for the case of a wave propagating over a seabed, which consists of ripples superimposed on an otherwise slowly varying mean depth, that satisfies the mild-slope equation. The vertical integration process is applied to the equation that is derived by Kirby, which is called the extended mild-slope equation. Tasy et al. [4] have subsequently followed Kirby's work to develop a finite element method (FEM) model. Massel [5] has derived two forms of the refraction–diffraction equation that are based on the Galerkin eigenfunction method with different weighting functions. In addition, he has suggested that the extended equation can be employed to model wave interactions with rapidly undulating topography (such as a sinusoidal seabed) in which the curvature term is not small compared to other terms in the equation. Chamberlain and Porter [6] have proposed a modified mild-slope equation (MMSE) that contains the curvature and the slope-squared terms by utilizing the variation principle and the Galerkin method. It is notable that the most important aspect of Chamberlain and Porter's improvement is in retaining a term involving the second derivatives of the quiescent depth, h. In addition, Porter and Staziker [7] have derived the corresponding jump condition that ensures mass conservation where the bed slope is discontinuous. Furthermore, they have also pointed out that a similar higher-order approximation, which has been proposed by Massel [5], is deficient because conservation of mass

* Corresponding author. Tel.: +886 4 26318652 4115; fax: +886 4 26525245.
E-mail address: wen1558@sunrise.hk.edu.tw (C.-C. Wen).

0955-7997/$ - see front matter Crown Copyright © 2009 Published by Elsevier Ltd. All rights reserved.
doi:10.1016/j.enganabound.2009.06.002

is violated. The appearance of $\nabla^2 h$, where ∇ is the gradient operator, in the MMSE implies that matching conditions must be applied to the dependent variable when ∇h is discontinuous. This means that the classical mild-slope equation fails to preserve mass conservation due to the discontinuity in the bed slope and leads to predictions with less accuracy. A similar work has been conducted by Chandrasekera and Cheung [8]. They have derived an alternative mild-slope equation that includes the bottom curvature and the slope-squared terms. The equation applies the hybrid element method to simulate wave reflection from ripple-beds and wave transformation over a circular shoal. Hsu and Wen [9] have developed a time-dependent parabolic model that not only includes the higher-order bottom-effect terms but also the energy dissipation terms. Cho and Kim [10] recast the elliptic MMSE into the form of a pair of hyperbolic first-order equations and utilize the internal wave generation technique to simulate wave propagation in an annular entrance channel. Silva et al. [11] have developed a numerical model for the elliptic MMSE that includes the energy dissipation term and have presented results for problems that involve arrays of cylinders between which the quiescent depth is allowed to vary. More recently, Chamberlain [12] has conducted a series of numerical tests on the scattering of water waves by a finite array of axisymmetric structures. This investigation is similar to Silva's works, but the aim of Chamberlain's work is restricted to depth profiles that include submerged islands, surface-piercing cylinders and their combinations. Nearly, all of the studies that are mentioned above indicate that the higher-order bottom terms (including the curvature and the slope-squared terms) cannot be neglected, especially under the intermediate water depth condition. Based on the above statements, the most frequently used numerical methods for wave scattering and diffraction are the finite difference method (FDM) and the FEM, which can be classified together as the domain method. The FDM is a classical and straightforward approach that is used to numerically solve the partial differential equation (PDE), while the FDM consists of transforming the continuous domain of the state variables by a network or mesh of discrete points. The PDE is converted into a set of finite difference equations that can be solved if they are subject to the appropriate boundary conditions. Unfortunately, the FDM often cannot fit complex geometry boundaries very well. On the contrary, a major advantage of the FEM is that it can easily handle complicated geometries. However, for the computation domain that is involved in an exterior-radiation problem, which is unbounded by nature, the discretization by the FEM has to be truncated somewhere. Hence, the Sommerfeld [13] radiation condition at infinity should be used. The non-reflecting boundary can be specified on the far-field boundary. As a result, its drawback is that the so-called far-field boundary has to be sufficiently distant from the radiating source. Furthermore, since the FEM requires internal meshes that are densely placed near the area of interest, the FEM meshes must be re-done even for minor changes in geometry in order to satisfy the element compatibility requirements.

However, with the boundary element method (BEM) that is based on Green's second identity, an n-dimension problem can be reduced to an $(n-1)$-dimension problem. Due to the fact that the dimensions of the problem that we are interested in are reduced, a smaller, linear algorithmic system is obtained, which leads to more efficient computations by requiring less computer memory. Differing from the previous two domain methods, the BEM distinguishes itself as a boundary method. Since the interior mesh does not have to be dealt with, the mesh preparation of the BEM is more cost efficient. The most important feature of the BEM is that it can automatically handle the Sommerfeld [13] radiation condition at infinity by adapting the governing equation of the Helmholtz equation. Then, the boundary integration equation, which is only valid under the no-flow condition, can be obtained. In reality, the solutions of the Helmholtz equation in polar coordinates are $H_n^{(1)}$ and $H_n^{(2)}$, which represent the outgoing and incoming waves, respectively. The Hankel function, $H_n^{(1)}$, fulfills the Sommerfeld [13] radiation condition, but $H_n^{(2)}$ does not. Fortunately, the outgoing wave that is present in the Helmholtz equation is also the foundational solution of the Helmholtz equation, which allows the infinite boundary condition to be automatically satisfied. With these advantages, the BEM has indeed recently become an essential part of the numerical tools, especially for infinite problems. Instead of the conventional hybrid method that is applied to the analytical solution in the exterior region, many numerical models take advantage of the BEM to develop mesh-free models in the exterior region because it automatically meets the Sommerfeld [13] radiation condition at infinity.

The BEM numerical models are rarely used for the variable-depth region. This is because the forcing terms will lead to the integral equation that involves complex domain integration. In order to overcome this deficiency, a powerful numerical technique, the dual reciprocity boundary element method (DRBEM), which transforms domain integrals into the corresponding boundary integrals for the non-homogeneous governing equation, has been proposed by Nardini and Brebbia [14]. This method adopts an approximating function, which is called the radial basis function (RBF), in domain integrating terms and applies Green's second identity to simplify the domain integration for the boundary integration. Using the DRBEM enables one to obtain "boundary-only" formulations for non-homogeneous, nonlinear and time-dependent problems by eliminating the domain integral that typically occurs in integral equation approaches.

To the best of the author's knowledge, the mild-slope equation that is solved by the BEM has been rarely used. Zhu [15] first developed a DRBEM wave model to study the combined reflection and diffraction of water waves propagating around islands or offshore structures over a varying seabed. Furthermore, the GDRBEM has been proposed by Zhu et al. [16] and focuses on the wave run-up from a tsunami. More recently, the PDRBEM [17] has been developed to study weakly nonlinear wave run-up around an island. Even if a number of numerical methods can be applied to solve the partial difference equations, the numerical solution of these problems is still under active research. Indeed, the application of existing MSE solutions, which use BEM, to practical engineering problems is still limited by the requirement of slowly varying bathymetry.

The purpose of this paper is to present an improved DRBEM wave model that is governed by MMSE and to demonstrate water wave scattering by an axisymmetric island structure that is mounted on a circular shoal with different topographies. The problem area includes the possibility of two kinds of basic topographies, which include types 1 and 2 cubic islands. In addition, combinations of the cubic island and ripple-beds are also considered in this study. A numerical approach, which shows the importance of curvature, is used to obtain the slope-squared terms. Following the tests, a discussion is presented on which extended terms that describe the topography can be neglected.

2. Formulation

2.1. Wave theory

In this paper, the fluid is assumed to be incompressible and inviscid while the flow is assumed to be irrotational. Thus, the fluid can be expressed in terms of the velocity potential, $\Phi(x,y,z,t)$,

which satisfies the Laplace equation within the whole domain

$$\nabla_h^2\Phi(x,y,z,t)+\frac{\partial^2\Phi(x,y,z,t)}{\partial z^2}=0, \tag{1}$$

where $\nabla_h{}^2() = (\partial^2()/\partial x^2)+(\partial^2()/\partial y^2)$. The three-dimensional problem is defined with a right-handed Cartesian coordinate system (x,y,z) in which x and y denote the horizontal Cartesian coordinates while z is measured vertically upward from the still water level. According to the linear wave theory, a harmonic wave train can be removed from the velocity potential, $\Phi(x,y,z,t)$, which describes the wave motion, by setting

$$\Phi(x,y,z,t)=\varphi(x,y,t)f(z), \tag{2}$$

where $f(z)$ is provided by $f(z)=\cosh k(h+z)/\cosh kh$ and $\varphi(x,y,t)$ is a complex function. The wave number, k, satisfies the linear dispersion relation $\omega^2=gk\tanh kh$, where ω is a given angular frequency and g the gravitational acceleration. Now, by following the method of Smith and Sprinks [18] and by applying Green's second identity to $f(z)$ and $\varphi(x,y,t)$, we have

$$\int_{-h}^{0} f(z)\nabla_h^2\varphi+\varphi f(z)_{zz}\,dz=-[f(z)\varphi_z-\varphi f(z)]_{z=-h}^{z=0}. \tag{3}$$

Upon substitution of $f(z)$ and the use of the following formulation $\nabla_h\Phi=f(z)\nabla_h\varphi+\varphi\nabla_h f(z)$, $\nabla_h{}^2\Phi=f(z)\nabla_h{}^2\varphi+2\nabla\varphi\cdot\nabla_h f(z)+\varphi\nabla_h{}^2 f(z)$, the dispersion relation and the relation $(\partial^2 f(z)/\partial z^2)=k^2 f(z)$ together with the linear free surface boundary conditions of

$$\frac{\partial^2\Phi}{\partial t^2}+g\frac{\partial\Phi}{\partial z}+=0 \text{ on } z=0, \tag{4}$$

the seabed boundary condition can be expressed as

$$\frac{\partial\Phi}{\partial z}+\left(\frac{\partial\Phi}{\partial x}\frac{\partial h}{\partial x}+\frac{\partial\Phi}{\partial y}\frac{\partial h}{\partial y}\right)=0 \text{ on } z=-h(x,y). \tag{5}$$

By substituting the seabed boundary condition Eq. (5) and the free surface boundary condition Eq. (4) into Eq. (3), the following integrated equation can be obtained:

$$\int_{-h}^{0}[\varphi k^2 f^2(z)+\nabla_h^2\varphi f^2(z)+2f(z)\nabla_h\varphi\,\nabla_h f(z)+\varphi f^2(z)\nabla_h^2 f(z)]\,dz = \frac{1}{g}\left(\frac{\partial^2\varphi}{\partial t^2}+\omega^2\varphi\right)|_{z=0}-f^2(z)\nabla_h f(z)\,\nabla_h h. \tag{6}$$

Leibniz's rule and the harmonic form of the velocity potential, $\varphi(x,y,t)=-ag/\omega\cdot e^{iS}$, where $a(x,y)$ is the wave amplitude and $S=k_x x+k_y y-\omega t$, are applied to derive the linear wave theory, which leads to the relation $(\partial^2\varphi/\partial t^2)=-\omega^2\varphi$. Based on the chain rule, $\nabla f(z)$ and $\nabla^2 f(z)$ from Eq. (6) can be expressed as a function of $(\nabla h)^2$ and $\nabla^2 h$, respectively. By substituting all of the expanding terms mentioned above into Eq. (6), we have the modified mild-slope equation [6–8], which is written in the form

$$\nabla_h(CC_g\nabla_h\varphi)+[k^2CC_g+f_1(kh)g\nabla_h^2 h+f_2(kh)gk(\nabla_h h)^2]\varphi=0, \tag{7}$$

where $C=\omega/k$ is the phase velocity, $C_g=\partial\omega/\partial k$ the group velocity, $\nabla_h()=(\partial()/\partial x,\partial()/\partial y)$ the horizontal operator, and $(\nabla_h h)$ and $\nabla_h{}^2 h$ the bottom slopes and bottom curvatures in the x and y directions, respectively.

f_1 and f_2 are both functions of kh and take the following form [8]:

$$f_1(kh)=\frac{[-4kh\cosh kh+\sinh 3kh+\sinh kh+8(kh)^2\sinh kh]}{8\cosh^3 kh(2kh+\sinh 2kh)}-\frac{kh\tanh \nu kh}{2\cosh^2 kh}$$

$$f_2(kh)=\frac{\operatorname{sech}^2 kh}{6[2kh+\sinh 2kh]^3}[8(kh)^4+16(kh)^3\sinh 2kh -9\sinh^2 2kh\cosh 2kh+12kh(1+2\sinh^4 2kh)(2kh+\sinh 2kh)].$$

In order to investigate the characteristics of wave propagation over the uneven bottom that is described by the MMSE, we express the complex velocity potential as $\varphi=a(x,y)e^{iS(x,y,t)}$. Substituting this into Eq. (7), we then get

$$\nabla_h[CC_g\nabla_h a]-[CC_g a\nabla_h S]\nabla_h S +[k^2CC_g+f_1(kh)g\nabla_h^2 h+f_2(kh)gk(\nabla h)^2]a +i[(CC_g\nabla_h a)\nabla_h S+\nabla_h(CC_g a\nabla_h S)]=0. \tag{8}$$

In Eq. (8), the real and imaginary parts must be balanced separately. The real part directly becomes

$$(\nabla_h S)^2=\frac{\nabla_h^2 a}{a}+\frac{\nabla_h(CC_g)\nabla_h a}{CC_g a}+\frac{[k^2CC_g+f_1(kh)g\nabla_h^2 h+f_2(kh)gk(\nabla h)^2]}{CC_g}. \tag{9}$$

We see that the Eikonal equation of the geometrical optics approximation corresponds to the neglected third terms of right-hand side in Eq. (8). Those terms represent the diffraction effects. Furthermore, for the imaginary part, we get

$$CC_g a\nabla_h a\,\nabla_h S+a\nabla_h[CC_g a\nabla_h S]=0, \tag{10}$$

which is collapsed to yield

$$\nabla_h[a^2CC_g\nabla_h S]=0. \tag{11}$$

2.2. Numerical model

Here, the computation domain is divided into two sub-domains as shown in Fig. 1. The first one is the exterior sub-domain, which is a constant depth region and is composed of D_2, Γ_b and Γ_∞. The other one is the interior sub-domain, which has varying quiescent depths and is composed of D_1, Γ_b and Γ_a. Between the two sub-domains, a pseudo-interface, which is called the matching condition and has been proposed by Chen and Mei [19], is imposed to couple the pressure and velocity in these sub-domains.

We have assumed that the complex function, φ, can be expressed as $\varphi^i+\varphi^s$, where φ^i is the incident wave component and φ^s is the scattered wave component. In the exterior sub-domain, MMSE will reduce to the Helmholtz equation, and the incident wave, φ^i, will satisfy the Helmholtz equation while the governing equation of the exterior sub-domain reduces to Eq. (12)

$$\nabla^2\varphi_2^s+k_2^2\varphi_2^s=0, \tag{12}$$

where k_2 is the wave number corresponding to the constant depth and φ_2^s the scattered wave potential in the exterior sub-domain, D_2. Because the governing equation is the Helmholtz equation, the fundamental solution φ^* can be chosen as

$$\varphi^*=\tfrac{1}{4}H_0^{(1)}(k_2 r) \tag{13}$$

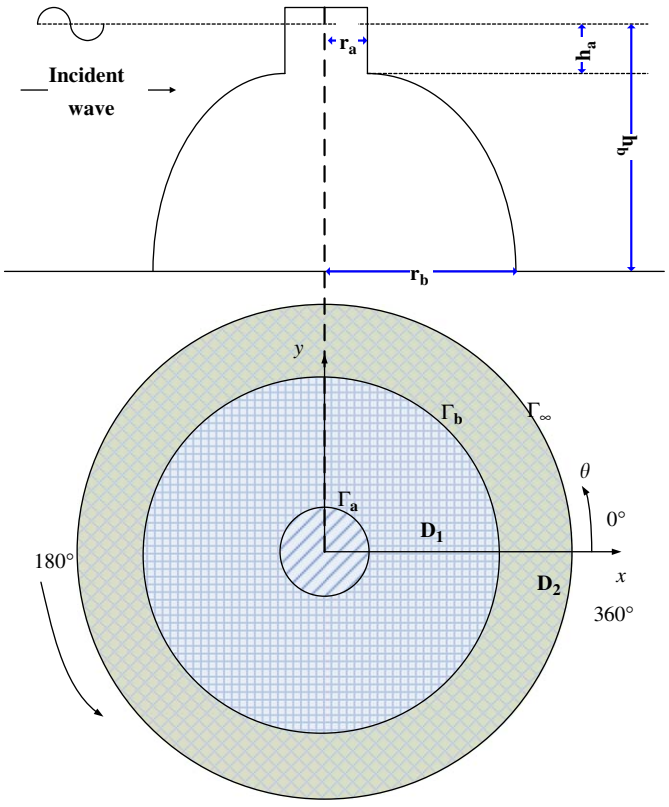

Fig. 1. Definition sketch.

where $H_0^{(1)}$ is a zero-order Hankel function of the first kind and r the Euclidean distance between a source and a field point. The conventional boundary element method can be adopted in the exterior sub-domain to solve the Helmholtz equation. The integration formula of the exterior sub-domain can be obtained after multiplying both sides of Eq. (13) by φ^*. By applying Green's second identity, the boundary integration formulation is subsequently obtained

$$c_{2i}\varphi_2^s + \int_{\Gamma_b+\Gamma_\infty} [\varphi_2^s q^* - \varphi^* q_2^s]\, d\Gamma = 0, \tag{14}$$

where $q^* = \partial\varphi^*/\partial n'$, $q_2^s = \partial\varphi_2^s/\partial n'$ and n' is the outer normal unit vector.

Since the fundamental solution of the Helmholtz equation is the Henkel function, the radiation condition at infinity (the so-called Sommerfeld [13] condition) is satisfied by the Hankel function

$$\lim_{r\to\infty}\sqrt{r}\left(\frac{\partial\varphi_2^s}{\partial r} - ik_2\varphi_2^s\right) = 0, r = \sqrt{x^2+y^2}. \tag{15}$$

It follows that one need only consider the boundary on Γ_a. Therefore, Eq. (14) can be simplified and rewritten as

$$c_{2i}\varphi_2^s + \int_{\Gamma_b} [\varphi_2^s q^* - \varphi^* q_2^s]\, d\Gamma = 0, \tag{16}$$

where c_{2i} is dependent upon the location of the source point on the boundary Γ_b.

If the boundary Γ_b is assumed to be smooth, the coefficient c_{2i} can be set to 0.5. It must be further noted that φ_2^s and q_2^s are all unknowns. This implies that Eq. (16) provides a relation between φ_2^s and q_2^s on the matching condition, and thus, it will be later substituted into the boundary integration equation of the interior sub-domain, D_1. Additionally, the given incident wave condition can be input by this approach.

In the interior sub-domain, D_1, the MMSE can be rewritten as

$$\nabla^2\varphi_1 + k_2^2\varphi_1 = (k_2^2 - k^2)\varphi_1 - \frac{f_1(kh)g\nabla^2 h}{CC_g}\varphi_1 - \frac{f_2(kh)gk(\nabla h)^2}{CC_g}\varphi_1 - \frac{\nabla CC_g\,\nabla\varphi_1}{CC_g}. \tag{17}$$

Green's second identity is applied to yield the following integration formulation:

$$c_{1i}\varphi_1 + \int_{\Gamma_a+\Gamma_b} [\varphi_1 q^* - \varphi^* q_1]\, d\Gamma = -\int_{D_1} b\varphi^*\, d\Omega, \tag{18}$$

where $b = (k_2^2-k^2)\varphi_1 - (f_1(kh)g\nabla^2 h/CC_g)\varphi_1 - (f_2(kh)gk(\nabla h)^2/CC_g)\varphi_1 - (\nabla CC_g\nabla\varphi_1/CC_g)$ and $c_{1i} = \begin{cases} 0.5 & \text{if } i\in\Gamma_a+\Gamma_b \\ 1 & \text{if } i\in D_1 \end{cases}$.

In the present work, the BEM can be used to solve this problem, but the corresponding domain integration will occur. This domain integration makes the numerical procedure difficult and causes the advantage of the BEM to be lost. Hence, the DRBEM is applied for the domain integration of Eq. (18). By employing the DRBEM, the right-hand side of Eq. (18) can be evaluated by transforming the domain integration into the equivalent boundary integration. This is achieved by expanding the function $b(x,y,\varphi)$ in terms of ξ, which is the radial basis function, at certain points chosen from the boundary (N+M) and the internal nodes (L) in the domain. The function $b(x,y,\varphi)$ can be expressed as

$$b(x,y,\varphi) = \sum_{k=1}^{N+L}\alpha_k\xi_k, \tag{19}$$

where $\xi_k = 1+r_k$ represents the interpolation function from a field node to an interpolating node and α_k is the undetermined corresponding interpolating coefficient. The essential goal of the DRBEM is to express ξ_k, which is a function of r_k, as a linear differential operator of a particular solution, φ_k. Thus, in the present work, ψ_k is chosen as the solution to

$$\nabla^2\psi_k + k_2^2\psi_k = \xi_k. \tag{20}$$

With the substitution for $b(x,y,\varphi)$ and the application of Green's second identity once again, the domain integration on the right-hand side of Eq. (18) is reduced to a boundary integration:

$$\int_{D_1} b\varphi^*\, d\Omega = \sum_{k=1}^{N+L}[-d_i\psi_{ik} + \int_\Gamma [\varphi^*\overline{\psi}_k - q^*\psi_k]\, d\Gamma]\alpha_k, \tag{21}$$

where d_i is also dependent upon the location of the source point. Finally, the boundary integration formulation for Eq. (18) becomes

$$c_{1i}\varphi_1 + \int_{\Gamma_a+\Gamma_b} [\varphi_1 q^* - \varphi^* q_1]\, d\Gamma = \sum_{k=1}^{N+L}\left[d_i\psi_{ik} - \int_\Gamma [\varphi^*\overline{\psi}_k - q^*\psi_k]\, d\Gamma\right]\alpha_k. \tag{22}$$

For the Helmholtz-type equations, the particular solution, ψ_k, for Eq. (20) has been determined by Zhu [15]. Since ξ_k is composed of the distance power series, Eq. (20) is equivalent to

$$\nabla^2\psi_k + k_2^2\psi_k = r_k^m, \tag{23}$$

where r_k is the distance between a source point k and a field point

x. A particular solution for Eq. (23) is found to be

$$\psi_k = \frac{\pi}{2}\left[Y_0(k_2 r_k)\int_0^{r_k} r^{m+1} J_0(k_2 r_k)\,dr - J_0(k_2 r_k)\int_0^{r_k} r^{m+1} Y_0(k_2 r_k)\,dr\right]. \tag{24}$$

After discretizing the boundaries Γ_a and Γ_b, Eq. (22) is applied consecutively for all of the nodes and yields a system of linear algebraic equations, which are arranged in the following matrix form

$$\mathbf{H}\varphi_1 - \mathbf{G}\mathbf{q_1} = (\mathbf{H}\psi - \mathbf{G}\overline{\psi})\xi^{-1}\left(\mathbf{K} + \frac{\mathbf{CC_{gx}}}{\mathbf{CC_g}}\xi_x\xi^{-1} + \frac{\mathbf{CC_{gy}}}{\mathbf{CC_g}}\xi_y\xi^{-1} + \mathbf{F_1} + \mathbf{F_2}\right)\varphi_1, \tag{25}$$

where **H** and **G** are composites of $h_{ij} = \int_{\Gamma_i}(\partial\varphi^*_{ij}/\partial n)\,d\Gamma$ and $g_{ij} = \int_{\Gamma_i}\varphi^*_{ij}\,d\Gamma$, respectively. In Eq. (25), φ_1 is the $(N+M+L)\times 1$ vector with the first N elements located on Γ_a, the next M elements located on Γ_b and the final L nodes located on the internal collocation points. Notice that the matching condition should be imposed on the N+1-*th*–M-*th* elements of the φ_1 vector in Eq. (25). The elements that are mentioned above contain the scattered potential and are different from the other elements of the φ_1 vector. Consequently, the mathematical matrix operation that yields a system of linear algebraic equations should be carefully performed, and the components of the resultant vector, which correspond to the boundary Γ_b, should be added to the incident wave potential. The definitions of **K**, ψ, $\overline{\psi}$, ξ^{-1}, ξ_x, ξ_y, $\mathbf{F}_1$, $\mathbf{F}_2$, $\mathbf{CC_g}$, $\mathbf{CC_{gx}}$ and $\mathbf{CC_{gy}}$ are all $(N+M+L)\times(N+M+L)$ matrices, which can be determined by following the DRBEM procedure. Details of this method can be found in Partridge et al. [20] and are therefore omitted here.

3. Model verifications

In order to verify a combined wave refraction and diffraction numerical model, analytical solutions are always preferable when examining the reliability of a numerical model. However, to the best knowledge of the authors, the analytical solution to the MMSE for the intermediate water depth condition is still lacking. Therefore, we calculate the conical island by MMSE under the long-wave condition to verify the case while reducing the bottom curvature term of the conical island and the effect of the bottom slope-squared term. Thus, the MMSE would approximate the MSE. Which would consequently allow the analytical solutions to be

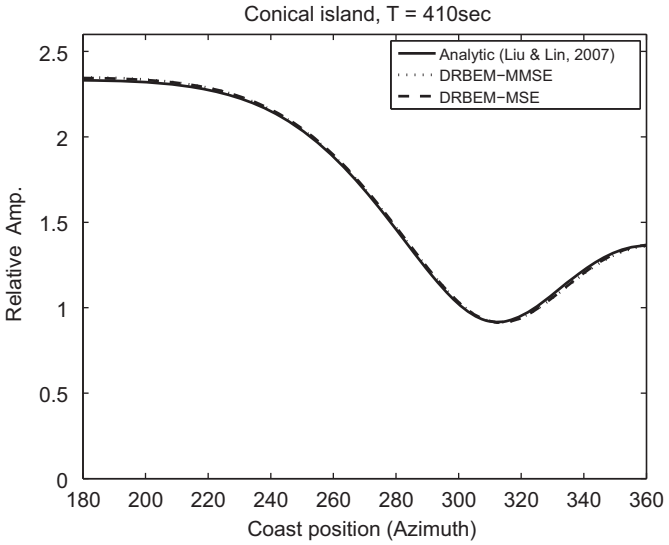

Fig. 3. Model verifications for the conical island along the sidewall.

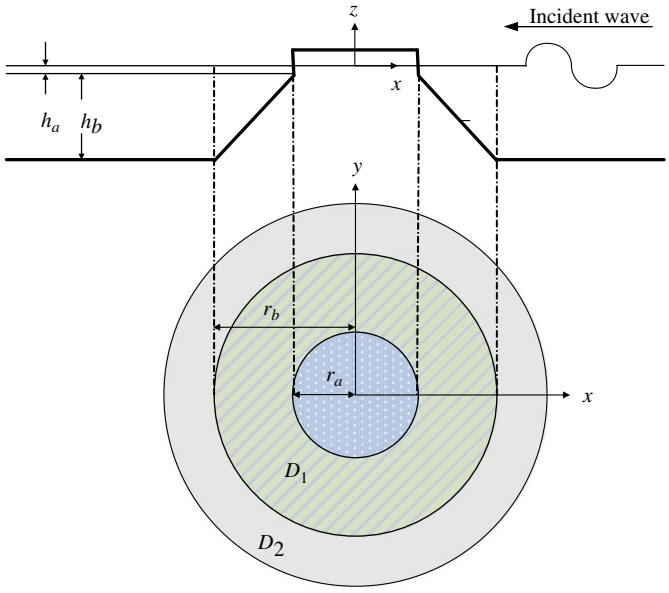

Fig. 2. Definition sketch of the conical island.

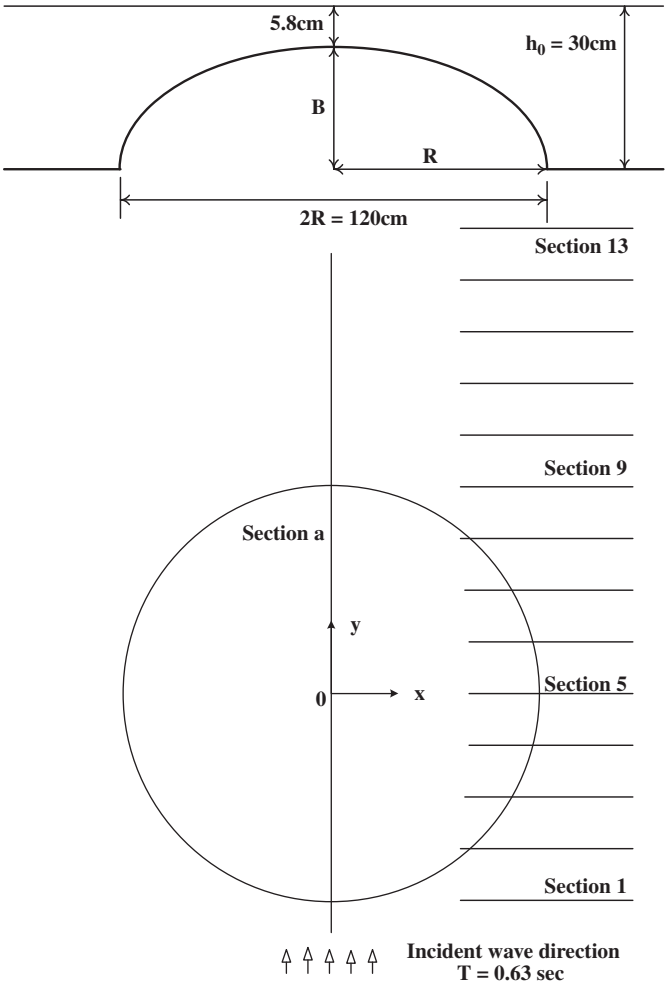

Fig. 4. Definition sketch of the experimental setup of Williams et al. [22].

compared with the numerical solutions of MMSE under the long-wave condition. Thus, we expect that the numerical solutions will coincide with the analytical solutions. In this section, the analytical solution of the MSE for the conical island, which has been proposed by Liu and Lin [21], will be compared to the numerical results.

A sketch of the conical island is shown in Fig. 2, where $h_a = 1333$ m, $h_b = 4000$ m, $r_a = 10{,}000$ m and $r_b = 30{,}000$ m. For the wave run-up along the sidewall of the island, Fig. 3 compares the present MMSE (including the reduction to the MSE) results to the analytical solutions. The numerical solution is obviously in well agreement with the analytical one. Notice that the wave period kh of 410 s ($k_b h_b = 0.3144$) at r_b is very close to the long-wave limitation.

The experimental data of the wave transformations over a submerged circular shoal that is surrounded by a region of constant water depth can be found in Williams et al. [22]. The bathymetry is represented in Fig. 4, where $R = 0.6$ m is the radius of the shoal, B the height of the shoal and h_0 the constant water depth. The experimental conditions are $B/R = 0.4$, $B/h_0 = 0.807$ and $kh_0 = 3.0$. The incident wave heights are conducted with a small wave steepness that ranges from 0.0041 to 0.0205. The dimensionless wave amplitude along the longitudinal section and over the center of the shoal is presented in Fig. 5. The results along the three cross-sections are displayed in Figs. 6–8. Cross-sections 8 and 13, which are, respectively, exhibited in Figs. 6 and 8, are the best matches between the experimental data and the results of the conventional FDM model. In great contrast to the conventional FDM model, the numerical results of the DRBEM–MMSE in all of the cross-sections exhibit excellent agreement with the experimental data; in fact, most of the data points that have been predicted by the model are in exact agreement. Although slight errors seem to have occurred closer to the center of the submerged circular shoal (see Figs. 5–8), they are certainly less

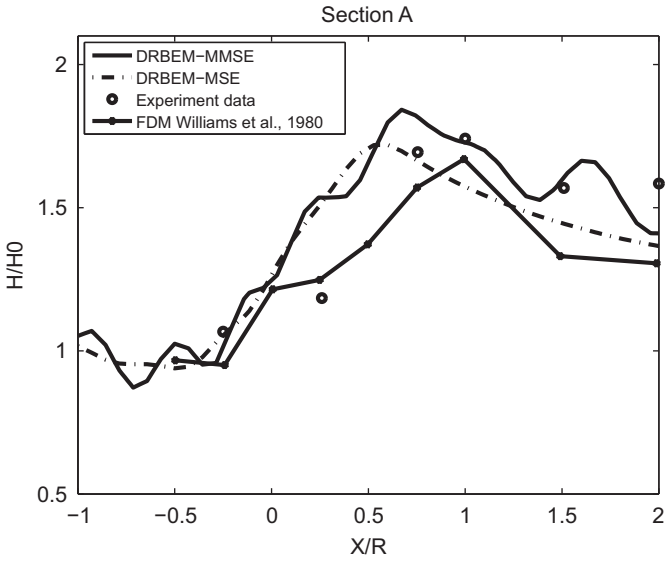

Fig. 5. Comparison of the computed wave heights with the experimental results of Williams et al. [22] along the section A.

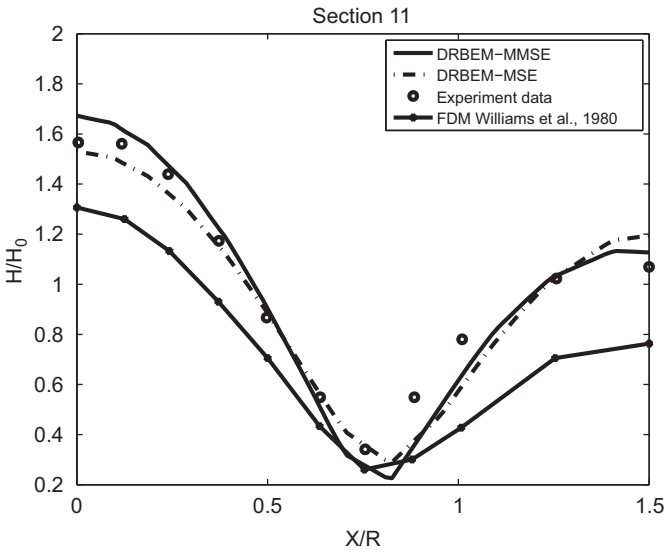

Fig. 7. Comparison of the computed wave heights with the experimental results of Williams et al. [22] along the Section 11.

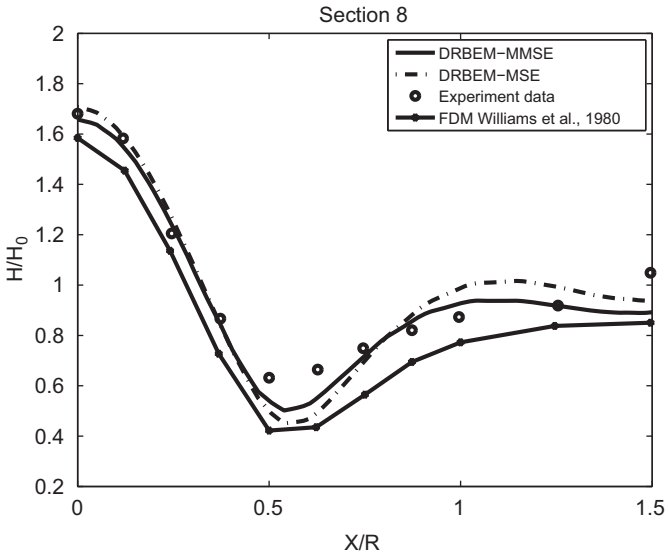

Fig. 6. Comparison of the computed wave heights with the experimental results of Williams et al. [22] along section 8.

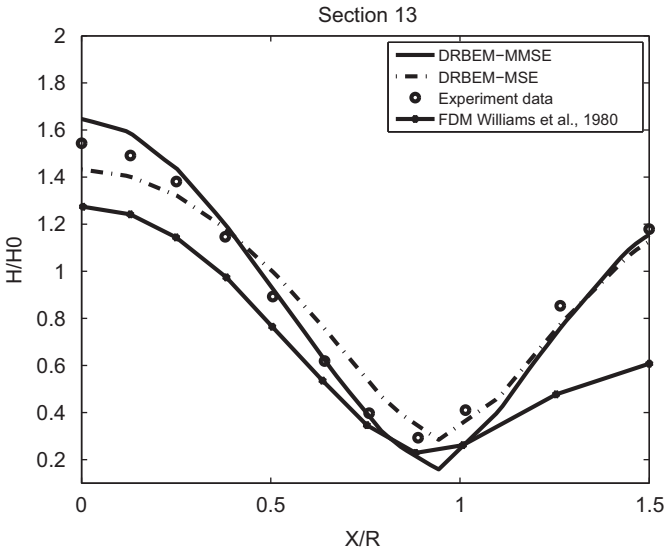

Fig. 8. Comparison of the computed wave heights with the experimental results of Williams et al. [22] along the section 13.

than those of the conventional FDM model. It is also important to note that when comparing the models to the experimental data, the DRBEM–MMSE model agrees better than the conventional MSE models. Moreover, the DRBEM–MSE model presents significantly better agreement than the conventional FDM model.

In the present study, the comparison between the three models can be evaluated by a benchmark. The agreement index, S_f, is defined as [23]

$$S_f = 1 - \frac{\sum_{i=1}^{N}(P_i - O_i)^2}{\sum_{i=1}^{N}(|P_i - \overline{O}| + |O_i - \overline{O}|)^2},$$

where P_i is the numerical value, O_i the observed value, $\bar{O}$ the mean value of the varieties of O_i and N the total measuring point at the control sections. The S_f values of all of the cross-sections are shown in Table 1 for comparison. Notice that as the indices approach unity, the accuracy results of the model improve. From Table 1, it is evident that the DRBEM–MMSE model has an agreement index that is more reasonable than those of the other models.

Table 1
The agreement indices for the cross-section of the numerical models.

Model/Section	Section-A	Section-8	Section-11	Section-13
DRBEM–MMSE	0.9693	0.9892	0.9874	0.9903
DRBEM–MSE	0.9615	0.9835	0.9840	0.9831
FDM—Williams et al. [22]	0.8909	0.9551	0.8956	0.9045

4. Results and discussion

In this section, two kinds of basic shoal profiles, cubic types 1 and 2, are applied to calculate the scattering of waves by a circular cylinder island that is mounted on those profiles (Fig. 9a). Based on the basic shoal profiles, the effects of the ripple-beds are also considered. In addition, the conical island is presented in Figs. 9 and 10 to show the difference between the conical island and the cubic islands. We assume two different types of bathymetry profiles and express them as a function of r to analyze the performance of the extended terms in the cubic island. The profile equations of the types 1 and 2 cubic islands are defined as the following equations, respectively: $y_1 = -5.0373 \times 10^{-10} \cdot r^3 + 1.797 \times 10^{-5} \cdot r^2 - 0.24174r + 680.32$

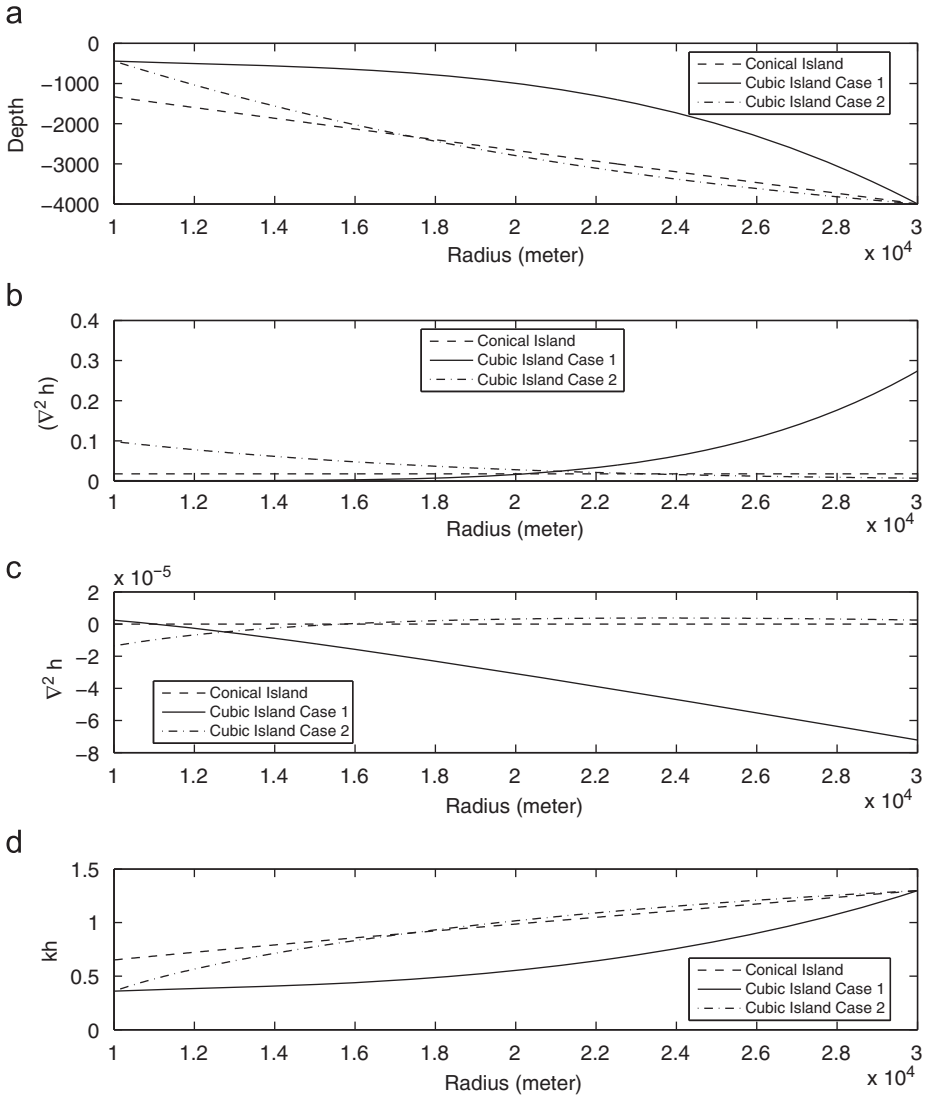

Fig. 9. Sketches of the parameters for all of the basic shoal profiles.

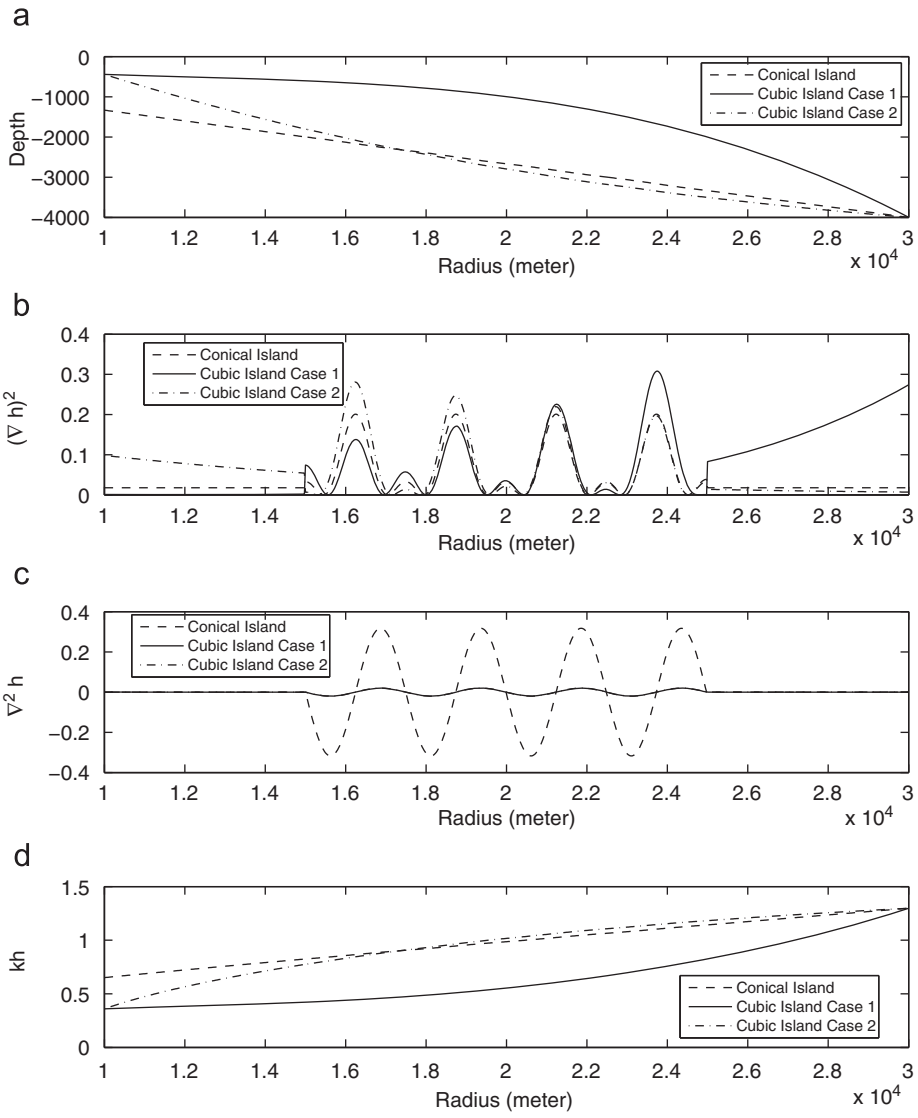

Fig. 10. Sketches of the parameters for all of the ripple-bed shoal profiles.

and $y_2 = -1.0373 \times 10^{-10} \cdot r^3 + 1.197 \times 10^{-5} \cdot r^2 - 0.52174r + 3680.3$. Additionally, the combination of the cubic shoals and the ripple-beds (Fig. 10a) will be discussed later. In order to examine the relative importance of the bottom curvature term and the bottom slope-squared term, the contributions of the bottom curvature ($f_1 g\nabla^2 h/CC_g$, MSE C) and the bottom slope-squared ($f_2 gk(\nabla h)^2/CC_g$, MSE S) terms are calculated and shown separately. The effects of the bottom curvature and the bottom slope-squared terms of these shoal profiles are presented in Figs. 9b, c and10b, c. In addition, Figs. 9d and 10d represent the corresponding kh of the topographies in order to realize the effects of $f_1(kh)$ and $f_2(kh)$ along the radius. It is noteworthy that the D/L_b value of the topography is 1.03. Furthermore, the coefficients of the curvature and the slope-squared terms are plotted in Fig. 11. It is clear that both $f_1(kh)$ and $f_2(kh)$ approach zero at the deep-water limitation and are most important in the intermediate water depth, while being somewhat important in the shallow water condition. However, the MMSE almost reduces to the MSE in both the deep-water and the very shallow-water limitation conditions. In order to emphasize the effects of the extended terms in the intermediate-depth waves, the wave period of the incident wave

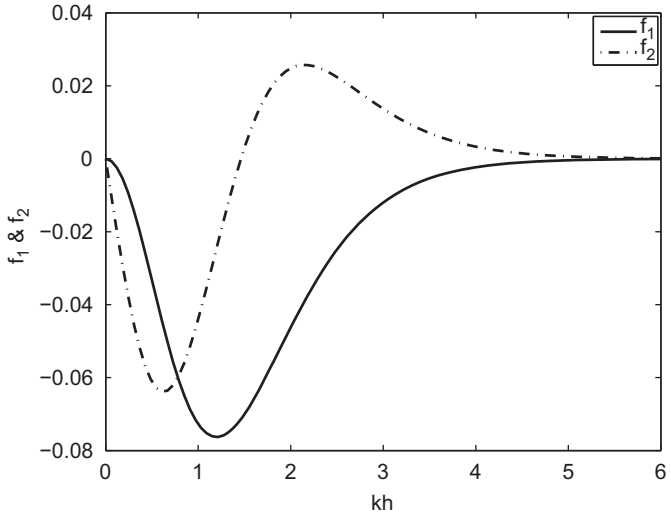

Fig. 11. Sketch of $f_1(kh)$ and $f_2(kh)$.

is set to 120 s, and the corresponding relative water depths are $k_b h_b = 1.3$ and $k_a h_a = 0.36$.

4.1. Type 1 cubic island

Fig. 12 shows the dimensionless wave amplifications along the sidewall of the type 1 cubic island for the four mild-slope models of this test problem. First, a comparison that we can make concerns predicting the behavior with respect to the position and magnitude of the wave height of the peaks. Almost all of the results appear to be in good agreement. One feature of this example is the fact that the decrease in the difference of the wave height between the MMSE and the MSE is more apparent for larger departures from the incident direction. Fig. 12 also indicates that the maximum wave amplitude always occurs in front of the island (180°) but, in this case, it shifts from the front side of the island to the lee side of the island (0°). The distribution of the dimensionless wave amplitudes in the MMSE and the MSE is displayed in Fig. 13. As expected, the results of the MMSE show a slight difference from the results of the MSE with a steep slope; however, this is only a minor effect. Fig. 14 presents this phenomenon and provides evidence to clearly support this explanation. For the MMSE model, a minor difference in the vicinity of $r = \pm 25{,}000$ m, which includes both bottom curvature and bottom slope-squared terms, is observed for a very steep slope where the effect of the bottom curvature and the bottom slope-squared terms becomes significant.

4.2. Type 2 cubic island

In this section, we discuss the numerical results of the type 2 cubic island, where the numerical experimental conditions are the same as the former case. In contrast with the type 1 cubic island, which has a slope tendency that is steep to gentle from offshore to the sidewall of the cubic shoal, the slope tendency of the type 2 cubic island is gentle to steep from offshore to the sidewall (see Fig. 9a). Fig. 15 graphically displays the wave amplification on the sidewall of the type 2 cubic island. Again, the results of all of the

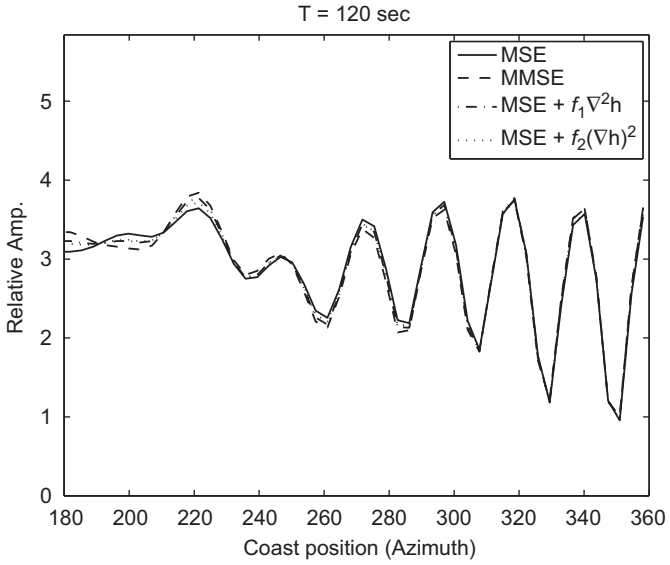

Fig. 12. Comparison of the type 1 cubic island along the sidewall.

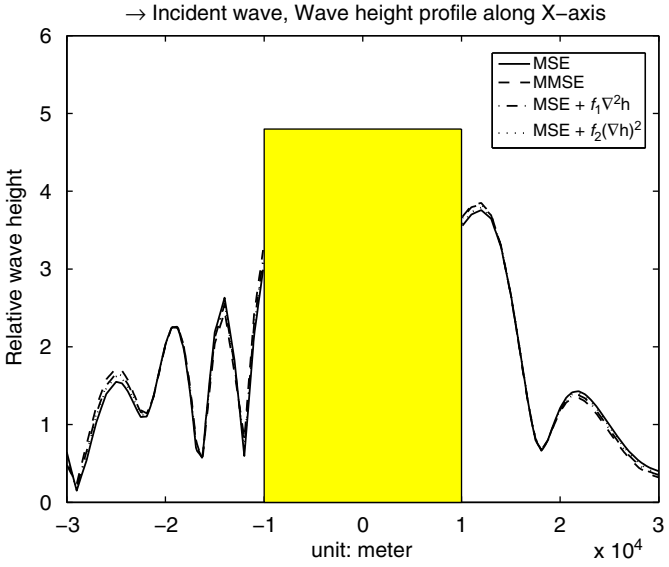

Fig. 14. Comparison of the type 1 cubic island at the intersection with $y = 0$.

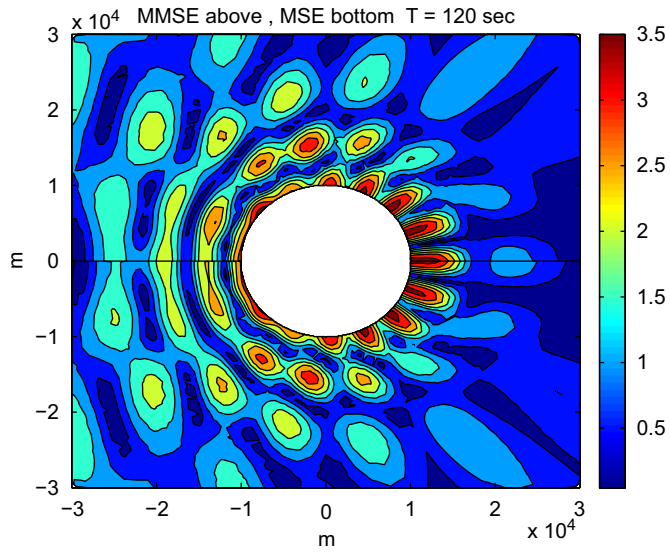

Fig. 13. Comparison of MMSE and MSE for the type 1 cubic island.

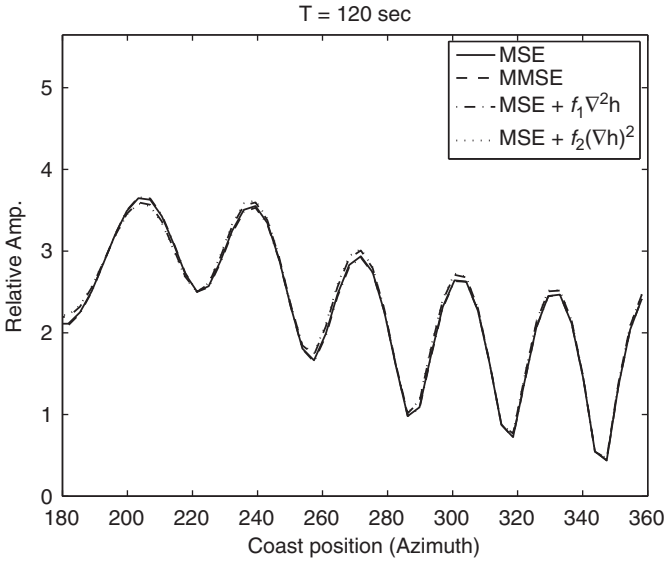

Fig. 15. Comparison of the type 2 cubic island along the sidewall.

models have similar behavior. As shown in this figure, the peak of the dimensionless wave amplitudes decreases periodically and continuously from 180° to 360°. The results of the MSE S model coincide with those of the MMSE model rather than others models, even though the discrepancies are less significant. Although the effects of the extended terms in the intermediate water depth ($k_b h_b = 1.3$) are strong, the phenomena that are observed in Fig. 15 still show fewer discrepancies. The comparison between the amplitudes of the dimensionless wave in the MMSE and MSE models is presented in Fig. 16. Obviously, the results of the MMSE and MSE models appear identical. Unlike Fig. 13, where the peaks of the dimensionless wave amplitudes that surround the island are denser, Fig. 16 exhibits peaks with dimensionless wave amplitudes that only occur in front of the island. In contrast with the front side of island, the dimensionless wave amplitudes in the lee side of the island, which is a shadow zone, are reduced because of the variation in the bathymetry and the effect of diffraction. It can be seen in Fig. 17 that in the front of the island the numerical results are supposed to coincide with each other;

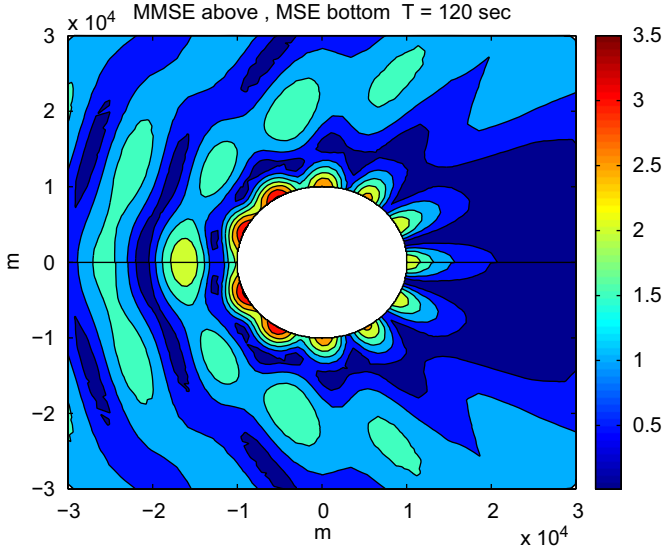

Fig. 16. Comparison of MMSE and MSE for the type 2 cubic island.

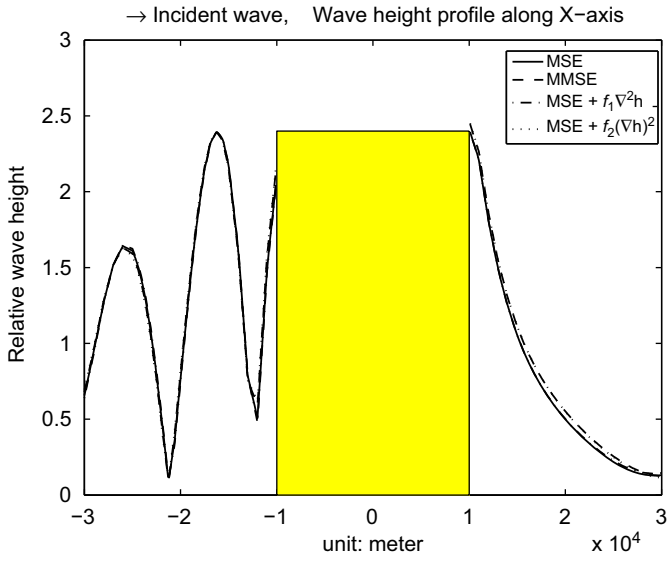

Fig. 17. Comparison of the type 2 cubic island at the intersection with $y = 0$.

however, on the lee side of the island, this is slightly violated. This can be attributed to the extended terms adding to the diffraction effect in the MMSE model, which includes the bottom curvature and the slope-squared terms that can describe the effect of wave diffraction. Eq. (9) can express the difference between the conventional wave refraction theory and the MMSE. Instead of the conventional wave refraction theory $(\nabla_h S)^2 = k^2$, the left-side term of Eq. (9), $(\nabla_h S)^2$of MMSE, also depends on the extended terms $f_1 g\nabla^2 h/CC_g$ and $f_2 gk(\nabla h)^2/CC_g$.

4.4. Effects of the ripple-beds

There are many previous works concerning wave propagation over uneven topography or ripple-beds. In this section, we have performed a literature survey [5–10]. Overall, the results of previous reports indicate that the bottom curvature and the slope-squared terms play an important role in improving the accuracy of the MSE and cannot be overlooked, especially for rapidly varying topography. Unfortunately, in the literature, there has been very limited study of wave scattering by island topography with ripple-beds. Thus, in this section, some numerical experiments on wave scattering by island topography with ripple-beds are conducted, and the disturbance of the ripple-beds is addressed by numerical experiments. In order to construct the ripple-beds, a sine function is combined by superposition to the cubic island profiles in the 15,000–25,000 m region. The amplitude of the sine curve is 5 m, and the period is 0.25π. The profiles of the two topographies can be expressed as the following functions of r:

$$y_1 = \begin{cases} -5.0373\times10^{-10}r^3 + 1.797\times10^{-5}r^2 - 0.24174r + 680.32; \\ 10000 < r < 15000 \text{ and } 25000 < r < 30000 \\ -5.0373\times10^{-10}r^3 + 1.797\times10^{-5}r^2 - 0.24174r + 680.32 + 5\sin(4\pi); \\ 15000 \le r \le 25000 \end{cases}$$

and

$$y_2 = \begin{cases} -1.0373\times10^{-10}r^3 + 1.197\times10^{-5}r^2 - 0.52174r + 3680.3; \\ 10000 < r < 15000 and 25000 < r < 30000 \\ -1.0373\times10^{-10}r^3 + 1.197\times10^{-5}r^2 - 0.52174r + 3680.3 + 5\sin(4\pi); \\ 15000 \le r \le 25000 \end{cases}$$

Fig. 18 shows the dimensionless wave amplitudes along the sidewall of the type 1 cubic island combined with the ripple-beds.

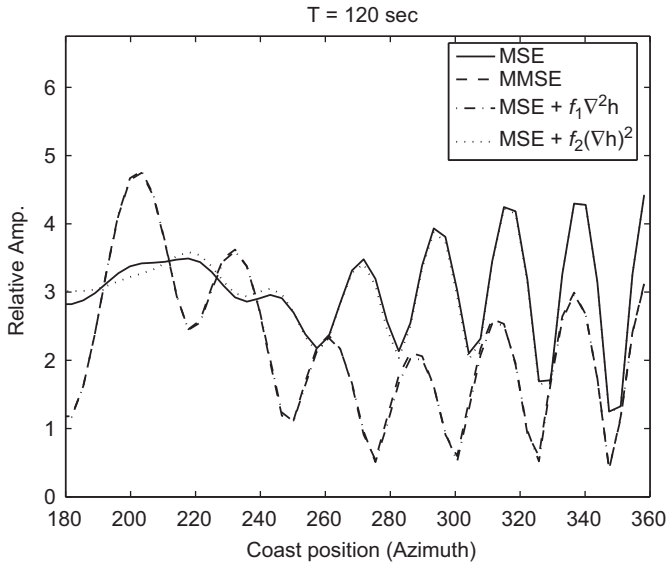

Fig. 18. Comparison of the type 1 cubic island with ripple-beds along the sidewall.

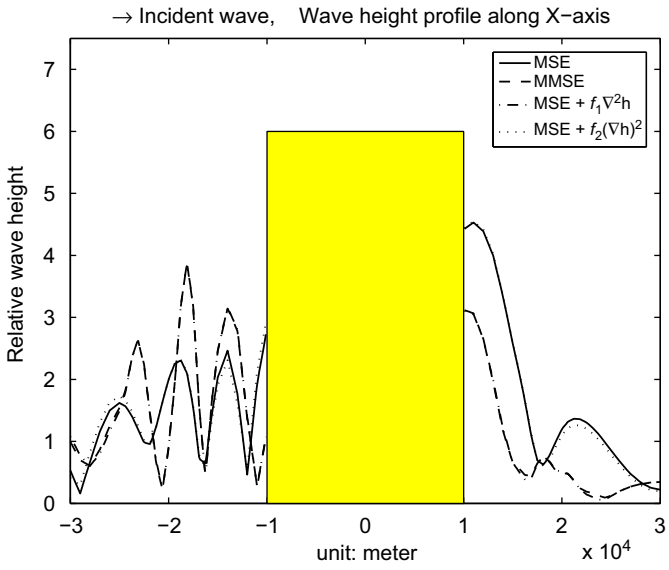

Fig. 19. Comparison of the type 1 cubic island with ripple-beds at the intersection with $y = 0$.

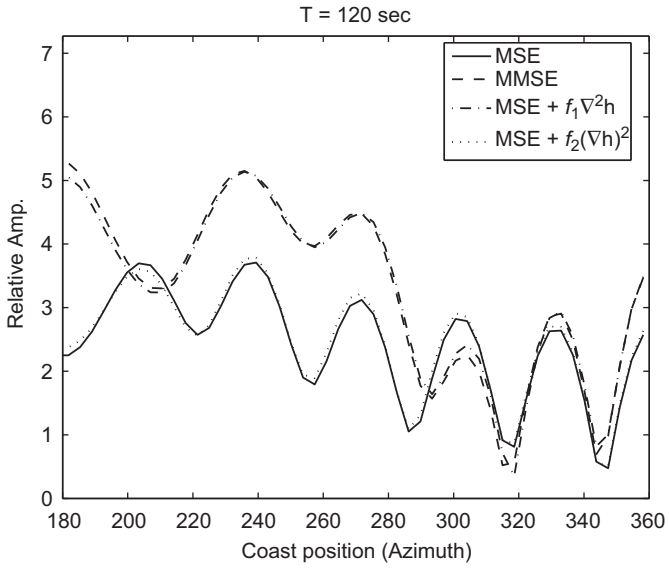

Fig. 20. Comparison of the type 2 cubic island with ripple-beds along the sidewall.

As shown in this figure, the wave phases of all of the solutions in the lee region of the island (310–360°) have similar behaviors, and the maximum difference occurs at 270°, where the magnitude is 2.9. Obviously, MMSE and MSE C coincide with each other, providing evidence that the bottom curvature term is dominant instead of the bottom slope-squared term. In addition, the dimensionless wave amplitude peak of the MMSE occurs in front of the island, which is in contrast with that of the MSE occurring on the lee side of the island. The overestimation of the MSE on the lee side of the island and the underestimation in the front of the island are also illustrated in Fig. 18. These findings support the previously reported claim [5–10] that if the curvature and the slope-squared terms are not accounted for, then accurate results for the rapidly undulating topographies are not possible. Fig. 19 depicts a comparison of the numerical results of the four models along the intersection with $y = 0$. Again, the predictions of the MSE C are similar to those of the MMSE. An interesting phenomenon that can be observed is the appearance of a peak in the MMSE occurring in the ripple-bed region. It must further be

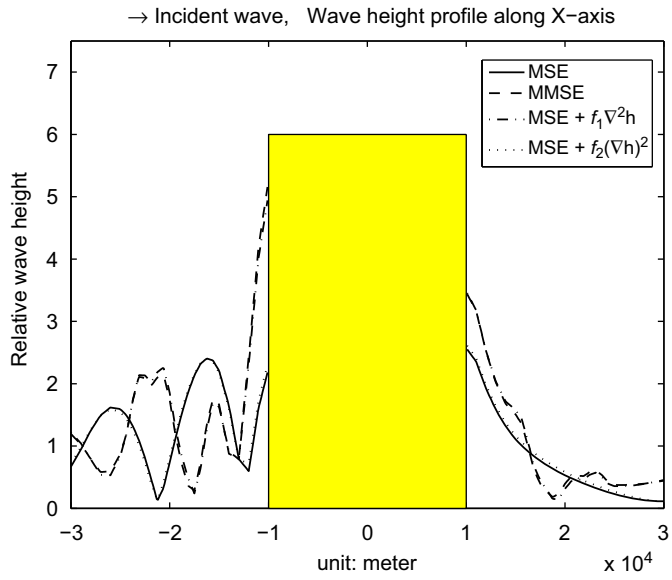

Fig. 21. Comparison of the type 2 cubic island with ripple-beds at the intersection with $y = 0$.

noted that the overestimation of the MSE along the sidewall in front of the island is 1.64. In other words, the magnitude of the MSE is almost 2.4 times that of the MMSE.

Figs. 20 and 21 show the results of the type 2 cubic island, where the shape of the shoal is taken to be a cubic polynomial with a negative tendency (Fig. 4a). Fig. 20 compares the dimensionless wave amplitude of different mild-slope models along the sidewall. Again, the incident wave condition is the same as in the previous cases. The solid line represents the results of the MSE case, the dashed line is for the MMSE case, the 'dash–dot' line is for the MSE C case, and the dotted line is for the MSE S case. Fig. 20 illustrates that all of the mild-slope models predict a similar position for the phase in the 240–360° region and that the maximum difference occurs at 181°, where the magnitude is 3.02. The MSE and MSE S models tend to underestimate the dimensionless wave amplitudes. This is because the dominant term, which is the bottom curvature term, is neglected in this model. Again, the findings show how important the extended terms are. Fig. 21 shows the dimensionless wave amplitudes at the intersection with $y = 0$. This figure shows that the position and magnitude of the dimensionless wave amplitudes that have been predicted by the MMSE are strongly affected by the ripple-beds that are located in the vicinity of $r = -22{,}000$. The wave height curve of the MMSE model in Fig. 21 shows a peak that is obviously affected by the ripple-beds; however, the MSE model does not show this. The difference in the dimensionless wave amplitude of the MMSE and the MSE on the sidewall is 3.02, while the magnitude of the MMSE is almost 2.3 times that of the MSE. The considerable difference may be due to the fact that the MSE model cannot respond to the effect of the wave refraction and diffraction attributed to the ripple-beds. Consequently, the oscillation in the region $r = 15{,}000$–$25{,}000$ m of the MMSE curve on the lee side of the island supports the claim that is reported above.

5. Conclusions

This investigation employs the modified mild-slope equation instead of the conventional mild-slope equation to improve the wave model via an integral numerical scheme, which is called the

dual reciprocity boundary element method. This model is evaluated by a series of cylindrical topographies that include the cubic island and the cubic island combined with ripple-beds. After several scenarios are addressed, the principal findings suggest that (1) the effects of the bottom curvature term and the slope-squared terms are small in smooth topographies; in other words, the MSE can provide acceptable numerical results in smooth topographies; (2) the effect of the bottom curvature term is dominant in the sinusoidal topography, while the bottom slope-squared term is small in all numerical experiments; (3) due to the neglect of the bottom curvature and the slope-squared terms in the MSE for the ripple-bed experiments along the sidewall, large differences in the corresponding dimensionless wave amplitudes of the MSE and the MMSE of almost 2.9 and 3.02 are found for the types 1 and 2 cubic islands, respectively; and (4) these findings support the notion that if the extended terms are not accounted for, then accurate results for rapidly undulating topography cannot be obtained.

Acknowledgements

This work was supported by the National Science Council, Republic of China under Contract number NSC 95-2221-E-019-082-MY2.

References

[1] Berkhoff JCW. Computation of combined refraction–diffraction. Proc 13th Conf Coast Eng ASCE 1972:471–90.
[2] Booij N. A note on the accuracy of the mild-slope equation. Coastal Eng 1983;7(3):191–203.
[3] Kirby JT. A general wave equation for waves over rippled beds. J Fluid Mech 1986;162(1):171–86.
[4] Tsay TK, Zhu W, Liu PLF. A finite element model for wave refraction diffraction, reflection, and dissipation. Appl Ocean Res 1989;11(1):33–8.
[5] Massel SR. Extended reflection–diffraction equation for surface waves. Coastal Eng 1993;19(1-2):97–126.
[6] Chamberlain PG, Porter D. The modified mild-slope equation. J Fluid Mech 1995;291:393–407.
[7] Porter D, Staziker DJ. Extensions of the mild-slope equation. J Fluid Mech 1995;300:367–82.
[8] Chandrasekera CN, Cheung KF. Extended linear refraction–diffraction model. J Waterw Port Coastal Ocean Eng 1997;123(5):280–6.
[9] Hsu TW, Wen CC. A parabolic equation extended to account for rapidly varying topography. Ocean Eng 2000;28(11):1479–98.
[10] Cho YJ, Kim GS. Internal generation of waves in fully elliptic modified mild-slope equation using source function method under FEM computational environment. Coastal Eng J 2004;46(4):425–40.
[11] Silva R, Borthwick AGL, Taylor RE. Numerical implementation of the harmonic modified mild-slope equation. Coastal Eng 2005;52(5):391–407.
[12] Chamberlain PG. Water wave scattering by finite arrays of circular structures. IMA J Appl Math 2007;72(1):52–66.
[13] Sommerfeld A. Partial differential equations in physics. New York: Academic Press; 1949.
[14] Nardini D, Brebbia CA. A new approach to free vibration analysis using boundary elements. In: Brebbia CA, editor. Boundary element methods in engineering. Berlin: Springer; 1982.
[15] Zhu SP. A new DRBEM model for wave refraction and diffraction. Eng Anal Boundary Elem 1993;12(4):261–74.
[16] Zhu SP, Liu H-W, Chen K. A general DRBEM model for wave refraction and diffraction. Eng Anal Boundary Elem 2000;24(5):377–90.
[17] Zhu SP, Liu HW, Marchant TR. A perturbation DRBEM model for weakly nonlinear wave run-ups around islands. Eng Anal Boundary Elem 2008;33(1):63–76.
[18] Sprinks T, Smith R. Scale effects in a wave-refraction experiment. J Fluid Mech 1983;129:455–71.
[19] Chen HS, Mei CC. Oscillations and wave forces in a Man-made Harbor in the open sea. TR no. 190, Ralph M. Parsons Laboratory, Department of Civil Engineering, MIT, 1974.
[20] Partridge PW, Brebbia CA, Wrobel LC. The Dual Reciprocity Boundary Element Method, Computational Mechanics Publications, Southampton Boston. Elsevier; 1992.
[21] Liu HW, Lin P. An analytic solution for wave scattering by a circular cylinder mounted on a conical shoal. Coastal Eng J 2007;49:393–16.
[22] Williams RG, Darbyshire J, Holmes P. Wave refraction and diffraction in a caustic region: a numerical solution and experimental validation. Proc Inst Civ Eng 1980;69:635–49.
[23] Willmott CJ. On the validation of models. Phys Geogr 1981;2:184–94.